

Annual Review of Condensed Matter Physics
 Shaping Capillary Solids
 from Statics to Dynamics

S.I. Tamim¹ and J.B. Bostwick²

¹Department of Mathematics, University of North Carolina at Chapel Hill, Chapel Hill, North Carolina, USA

²Department of Mechanical Engineering, Clemson University, Clemson, South Carolina, USA; email: jbstwi@clemson.edu

ANNUAL
REVIEWS **CONNECT**

www.annualreviews.org

- Download figures
- Navigate cited references
- Keyword search
- Explore related articles
- Share via email or social media

Annu. Rev. Condens. Matter Phys. 2025. 16:173–94

First published as a Review in Advance on November 4, 2024

The *Annual Review of Condensed Matter Physics* is online at conmatphys.annualreviews.org

<https://doi.org/10.1146/annurev-conmatphys-043024-084829>

Copyright © 2025 by the author(s). This work is licensed under a Creative Commons Attribution 4.0 International License, which permits unrestricted use, distribution, and reproduction in any medium, provided the original author and source are credited. See credit lines of images or other third-party material in this article for license information.



Keywords

capillarity, elasticity, soft materials, two-phase system, surface and interfacial phenomena, interfacial instability, pattern formation

Abstract

The shape of a soft solid is largely determined by the balance between elastic and surface energies with capillarity becoming important at length scales smaller than the elastocapillary length, which approaches the millimeter scale for the softest hydrogels, leading to many new and surprising phenomena. This review is focused on describing recent experimental and theoretical progress on the deformations of soft solids due to capillarity in two-phase systems for both statics and dynamics. Relative to rigid solids, surface tension can lead to the rounding of sharp corners, wrinkling and creasing, and general morphological shape change of the static equilibrium configuration, beyond a critical elastocapillary number. With regard to dynamics, both surface tension and viscoelasticity affect wave number selection in a number of dynamic pattern formation phenomena in soft solids, such as elastocapillary-gravity waves, Rayleigh–Taylor instability, Plateau–Rayleigh instability, Faraday waves, and drop oscillations, all of which have direct analogs with classical hydrodynamic instabilities helping to interpret the relevant physics.

1. INTRODUCTION

The shape of a material object often determines functionality. This is seen in a wide range of materials from the design of metal heat sinks critical for electronic cooling (1) and gas turbine blades for efficient heat transfer (2) to morphogenesis and the formation of highly corrugated biological tissue structures seen in the sulci of the brain cortex (3) and placental villous tree (4) that sustain and create life, to the shape of liquid interfaces that facilitate the assembly of particles and cells (5, 6) in tissue engineering applications (7) and precede the atomization of life-saving medicines in drug delivery devices (8). These shapes can be static or dynamic and can be harnessed to fabricate complex structures in soft matter (9–11). The interfacial physics and associated coupling with the bulk material response become critically important in determining the shape of soft solids and are the topic of this review.

Rigid solids can take on largely any shape as the undeformed configuration is a minimum of the elastic energy, whereas liquids, due to capillarity, tend toward a spherical shape in order to minimize surface energy. Soft solids, such as gels and biological tissues, can have elastic and surface energies that are of the same order of magnitude, but the question is on what length scale L . Simple dimensional analysis yields the elastocapillary length $\ell_e = \sigma/\mu$ as the elastic energy is proportional to material volume and surface energy to material surface area, with σ being the surface tension and μ being the elastic shear modulus. The elastocapillary length can range from the atomic scale for metals $\ell_e \sim 10^{-11}$ m to the micron scale for elastomers $\ell_e \sim 10^{-6}$ m, to the millimeter scale for hydrogels $\ell_e \sim 10^{-3}$ m. The physical interpretation of the elastocapillary length is that systems with characteristic length L (either intrinsic or imposed) are dominated by elastic effects when $L > \ell_e$ or capillary effects when $L < \ell_e$, and a transition occurs when $L \sim \ell_e$, as schematically illustrated in **Figure 1** using the dimensionless elastocapillary number $\Sigma \equiv \ell_e/L = \sigma/\mu L$, which shows

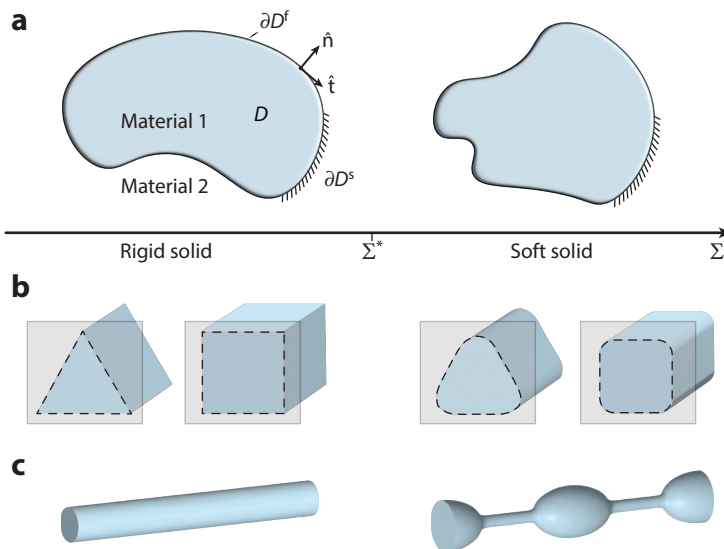


Figure 1

Illustration of the elastocapillary effect in a two-phase system, as it depends on the elastocapillary number Σ , contrasting the limiting cases of a rigid solid $\Sigma < \Sigma^*$ and soft solid $\Sigma > \Sigma^*$, with Σ^* being the critical elastocapillary number. (a) Schematic diagram of the two-phase system in which a free interface ∂D^f endowed with surface tension separates the domains of material 1 and material 2, which are partially fixed to a rigid container with geometry ∂D^s . Rigid solids can adopt nearly any shape, whereas capillary effects manifest themselves in soft solids by (b) rounding sharp corners and (c) inducing shape-change instabilities.

Morphogenesis:

the process by which a biological structure, i.e., cell, organ, tissue, develops its shape

Elastocapillary

length, ℓ_e : the ratio of surface tension σ to elastic shear modulus μ defines an intrinsic length scale $\ell_e = \sigma/\mu$

Elastocapillary

number, Σ :

a dimensionless number $\Sigma \equiv \ell_e/L = \sigma/\mu L$ that defines the balance of surface and elastic energies

the rounding of sharp edges and morphological shape change of a rigid cylinder due to capillarity, as prototypical examples. External loads, such as the gravitational body force or prescribed surface traction, naturally affect the equilibrium shape of a soft solid, but what seems less appreciated is how the dynamic material response of soft solids similarly affects pattern formation at interfaces.

Hydrodynamic instability is responsible for a number of canonical pattern formation phenomena, including shear-induced Kelvin–Helmholtz instabilities seen in clouds and other multilayer systems, Faraday waves (which appear as a parametric instability on a vibrated fluid layer), and the breakup of a fluid thread due to the Plateau–Rayleigh instability (PRI), to name a few. These systems are known for their aesthetic beauty. The signature of any instability is competing physics, as defined by characteristic forces, energies, or timescales. In recent years, it has been shown that soft solids are also susceptible to many classical hydrodynamic instabilities, but one must account for the additional physics associated with elasticity to determine the stability threshold and dominant wavelength describing the pattern formation.

Bulk elastocapillarity is restricted to two-phase systems, whereas elastocapillary phenomena are also readily seen in soft wetting phenomena, or three-phase systems, in which the liquid surface tension deforms the underlying substrate. Here, liquid surface tension can bend thin structures, e.g., capillary origami and the bundling of fibers, and form a wetting ridge on a semi-infinite substrate. To distinguish between such phenomena, the former is referred to as bendocapillarity. There is a significant amount of literature in these areas, and we refer the reader to the recent reviews by Bico et al. (12) for the former and Andreotti & Snoeijer (13) for the latter. For soft solids, the surface stress Υ and surface energy σ are generally not equal, as they are for liquids, and are related through the surface strain $\boldsymbol{\epsilon}$ by the Shuttleworth equation $\Upsilon = \sigma \mathbf{I} + \partial\sigma/\partial\boldsymbol{\epsilon}$ (14), as described in detail in the review by Style et al. (15) (see the sidebar titled Shuttleworth Effect). In fact, surface stresses in solids can be anisotropic and compressive. For the purposes of this review, we assume the surface stress is equal to the surface energy and refer to it as the surface tension hereafter.

This review is focused on capillary effects in soft solids for two-phase systems. Our discussion is pedagogical, beginning with static shape-change phenomena, and then moving on to dynamic pattern formation. In most phenomena we discuss, there is an analogous classical problem that appears as a limiting case that helps frame the problem and interpret the relevant physics.

2. STATICS

The static equilibrium shape of a soft solid is defined by the balance between the bulk elastic energy and free surface energy associated with capillarity. Using the general description of nonlinear

Wetting ridge: cusp-like shape formed on a soft substrate at the three-phase contact line due to the unbalanced liquid surface tension force

Bendocapillarity: the bending of thin elastic structures with bending modulus B by surface tension σ occurs at a characteristic length scale $\ell_b = \sqrt{B/\sigma}$

SHUTTLEWORTH EFFECT

Generally, surface stress is defined as the force per unit length required to deform the free surface. Shuttleworth (14) showed that the solid surface stress Υ is a function of the surface strain $\boldsymbol{\epsilon}$ as described by the relationship $\Upsilon = \sigma \mathbf{I} + \partial\sigma/\partial\boldsymbol{\epsilon}$ [see also Müller & Saúl (16) for a thermodynamic derivation of the free surface stress]. Although it is mathematically convenient and physically reasonable in many cases to assume surface stress to be a constant, it remains an approximation that needs to be critically assessed. A major difficulty in incorporating variable surface stress has been the lack of physical understanding of when the Shuttleworth effect becomes important. Studies on the deformation of soft gels by a line force at the three-phase liquid contact have shown a significant strain dependence on the surface stress (17, 18); but, in contrast, an experiment on a stretched elastomer found no strain dependence (19). This indicates the possibility of varied interpretations, even within similar experiments. This remains an active area of research.

Neo-Hookean material:

a hyperelastic material with nonlinear stress-strain constitutive law useful for describing finite amplitude deformations in cross-linked polymers, such as gels and rubbers

Young–Laplace equation:

an equation $\Delta p = \sigma \mathcal{H}$ relating the pressure jump Δp across a liquid interface to the local curvature \mathcal{H} there

continuum mechanics in a Lagrangian framework, the current position of a material point \mathbf{R} is a function of its reference position $\mathbf{r}(x, y, z)$, leading to the following mapping $\mathbf{R}(\mathbf{r}) = (X(x, y, z), Y(x, y, z), Z(x, y, z))$. For a neo-Hookean material typical of soft solids, the elastic energy of a volume D is described as (20)

$$E_{\text{el}} = \int_D d\mathbf{r} \left(\frac{\mu}{2} (\text{tr}(\boldsymbol{\varepsilon}) - 3 - 2 \ln J) + \frac{\lambda}{2} (\ln J)^2 \right), \quad 1.$$

where $F_{ij} = R_{ij}$ is the deformation gradient tensor and $J = \det(\mathbf{F})$ is its determinant, $\boldsymbol{\varepsilon} = \mathbf{F}\mathbf{F}^T$ is the strain tensor, and μ and λ are the Lamé parameters representing the shear and bulk modulus, respectively, which are related to one another through the Poisson ratio ν by $\lambda = 2\nu\mu/(1 - 2\nu)$. Capillarity enters through the surface energy,

$$E_{\text{cap}} = \sigma \int_{\partial D^f} \|(\mathbf{F}^{-1})^T \mathbf{n}\| ds, \quad 2.$$

where ∂D^f is the free surface, ds is the area element, and \mathbf{n} is the unit normal on the interface. The total energy then becomes $E = E_{\text{el}} + E_{\text{cap}}$. The first variation of total energy δE with respect to a small displacement $\delta \mathbf{R}$ leads to linear momentum conservation in the bulk domain D (21),

$$\nabla \cdot \mathbf{T} + \rho \mathbf{b} = \mathbf{0}, \quad 3.$$

and the boundary conditions at the free interface ∂D^f and solid support ∂D^s ,

$$\mathbf{n} \cdot \mathbf{T} \cdot \mathbf{n} = \sigma \mathcal{H}, \quad \mathbf{n} \cdot \mathbf{T} \cdot \mathbf{t} = 0[\partial D^f]; \quad \mathbf{U} = \mathbf{0}[\partial D^s]. \quad 4.$$

Here, \mathbf{T} is the Cauchy stress tensor, ρ is the density, \mathbf{b} is the acceleration due to body force (e.g., gravity), and \mathcal{H} is the curvature. The normal stress condition is similar to the Young–Laplace equation applicable in fluid interfaces (22–24). A shear-free condition is applied on the free surface ∂D^f and a zero-displacement condition on the support surface ∂D^s . For reference, the stress tensor for an isotropic linear elastic material can be written as $\mathbf{T} = \lambda \text{Tr}(\boldsymbol{\varepsilon}) + 2\mu \boldsymbol{\varepsilon}$.

The perspective we take in this review is to describe the self-induced deformations of the soft solid due to capillarity, relative to the unstrained configuration.

2.1. Capillary-Induced Instability

The presence of surface stress on a soft solid often results in morphological shape change in the form of localized sharp corners and edges, as seen in creasing and buckling (25). These shapes are typically understood as examples of interfacial instability in which, due to excessive surface stress, a small localized perturbation grows into a large deformation with associated localized geometry and spatial extent, i.e., pattern formation. The typical approach to analyze such instabilities begins with the consideration of a rigid undeformed solid with a smooth interface and no surface stress $\mathbf{R} = \mathbf{R}_0$. The base state is given a small perturbation of $O(\varepsilon) \ll 1$ such that $\mathbf{R} = \mathbf{R}_0 + \varepsilon \mathbf{R}_1$, and the stability problem is posed by taking the second variation of total energy $\delta^2 E$. When the base state is unstable, surface tension drives the material toward a secondary equilibrium state that differs from the base state.

2.1.1. Plateau–Rayleigh instability. It is well known that a cylindrical liquid column is susceptible to breakup into small droplets through the Plateau–Rayleigh instability (PRI) (26–28). Mora et al. (29) showed that agarose gel cylinders of radius R and shear modulus μ are susceptible to a similar instability that exhibits free surface undulations above a critical elastocapillary number $\Sigma_c = \sigma/\mu R = 6$, as shown in **Figure 2a**. In their experiments, the gel cylinders were cast

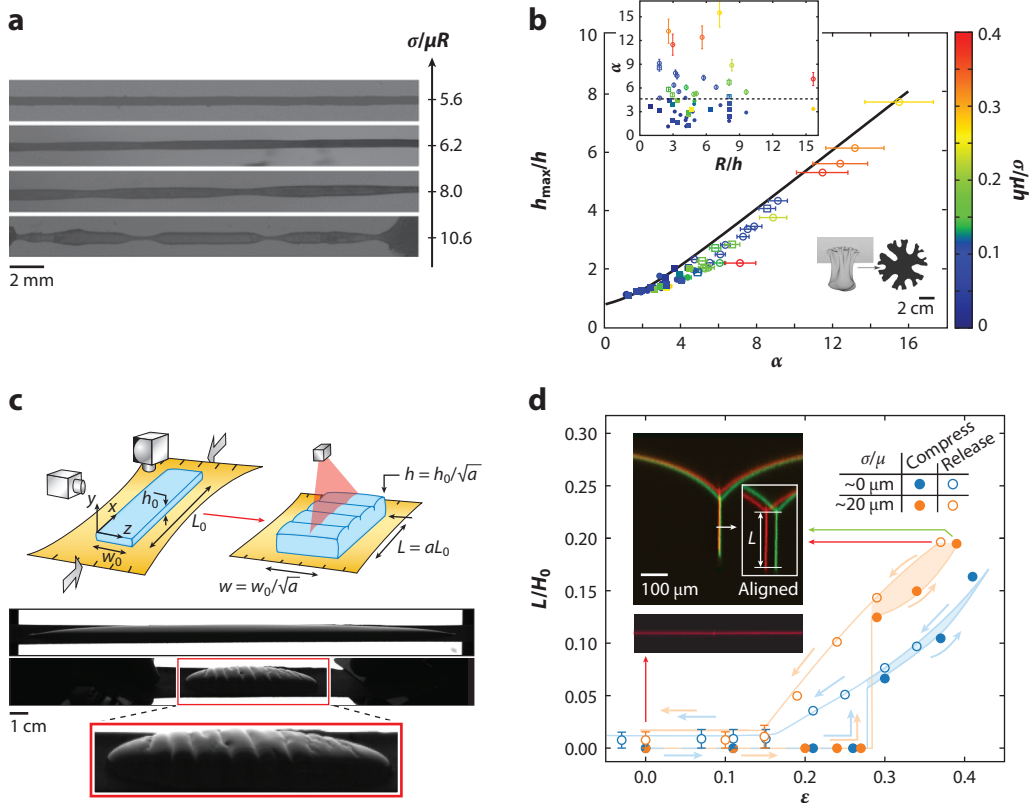


Figure 2

Equilibrium shapes of capillary solids. (a) Axial undulations of a cylinder of agar gel appear above a critical elastocapillary number $\Sigma = \sigma/\mu R > 6$ due to the Plateau–Rayleigh instability. (b) A hanging cylinder of aqueous polyacrylamide hydrogel will stretch to a length h_{\max} longer than its initial length h that depends on the elastogravity $\alpha = \rho g b/\mu$ and elastocapillary Σ numbers. Beyond a critical threshold, self-similar hierarchal wrinkles develop as shown in three-dimensional view and in a horizontal slice (*inset*). Here, solid and empty symbols denote axially symmetric and asymmetric deformations. (c) Uniaxial contraction of a soft gel ($\mu \approx 1$ kPa) leads to a Biot instability with corresponding surface wrinkling beyond a critical stretch amplitude a that depends on the elastocapillary number. (d) Compression-induced creasing of soft polymeric gels creates self-contact lines that show hysteretic behavior linked to elastocapillary effects, as seen by plotting the dimensionless self-contact length L/H_0 against the global strain ϵ for purely elastic ($\ell_e \approx 0$) and soft ($\ell_e \approx 20 \mu\text{m}$) materials. Panel a adapted with permission from Reference 29. Panel b adapted from Reference 30 with permission from the Royal Society of Chemistry. Panel c adapted from Reference 31 with permission from the Royal Society of Chemistry. Panels a–c provided by S. Mora. Panel d adapted from Reference 32 (CC BY 4.0); provided by S. Karpitscka and J. Snoeijer.

in polystyrene molds and placed in a toluene bath that dissolved the molds and exposed the gel to a surface tension that initiated the instability. For $\Sigma > \Sigma_c$, the deformation increases with a power-law relation, suggesting this is a threshold instability. To explore large amplitude behavior beyond the instability threshold predicted from linear theory, numerical and theoretical models have been proposed to account for the nonlinear material response of neo-Hookean solids, focusing on the roles of axial stretch, boundary conditions, and system configuration, e.g., hollow cylinders (33–35). Xuan & Biggins (36) showed that PRI in solids is fundamentally different than in liquids and leads to a phase separation between two distinct regions of stretch that gives rise to rich postcritical morphologies, such as necking, ballooning, and bead-on-string structures that can be observed in elastic fibers and tubes (37–40).

Self-similar:

a feature that looks the same at different magnifications, as seen in fractals

Hierarchical

patterns: spatial patterns that exhibit distinct subfeatures at different length scales

Microtomography:

an experimental technique used to image cross sections of a sample by interpreting the interference patterns of a penetrating wave

2.1.2. Creasing and wrinkling. An elastic solid subject to a uniaxial compressive strain becomes unstable to sinusoidal perturbations, as described by Biot (41), who predicted the critical stretching threshold for a semi-infinite elastic half-space. The lack of an intrinsic length scale in Biot's analysis made comparison with experiments difficult because many wavelengths are unstable beyond a critical strain, and a dominant wavelength cannot be identified. This can be resolved by accounting for the length scales associated with the (a) surface curvature and (b) the finite thickness of the solid. Experiments were performed with strained bridged microemulsion gels with shear modulus $\mu \sim 1$ kPa to create the surface creasing patterns, shown in **Figure 2c**, above a critical stretch threshold related to the elastocapillary number, thus resolving the missing length scale in Biot's theory (31, 42).

Free surface creasing of a solid is defined by the formation of self-contact regions that grow from a nucleation site and is ubiquitous in polymeric soft gels and growing biological tissues (43, 44). The review article by Dervaux & Amar (45) provides a comprehensive discussion of the creasing instability focusing on the morphology of soft polymeric materials. Notably, surface tension effects give rise to hysteretic bistable behavior under compression, whereby existing creases do not disappear at the same strain value as they appear (46). This is seen in experiments in which a soft polymeric gel undergoes cyclic folding–unfolding via periodic modulation of the global compressive strain, which leads to a shape asymmetry between the folding and unfolding regimes that is attributed to contact-line self-pinning, as shown in **Figure 2d** (32). Finite element analysis of the crease morphology in soft materials has revealed self-similar shapes due to the combined effects of surface tension and adhesion (47).

Other complex spatial patterns, such as wrinkles, can similarly appear in soft solids when surface tension interacts with other forces, such as the self-weight due to gravity. Mora et al. (30) have studied the shape of a hanging elastic cylinder of polyacrylamide hydrogel whose axis is aligned with the gravity vector. Above a critical value of the control parameters, the cylinder can simultaneously undergo bulk axial stretching along its length that is accompanied by self-similar hierarchical patterns that appear around the perimeter of the cylinder, as shown in **Figure 2b**, which are measured using microtomography. As the substrate becomes softer, both gravitational and surface tension effects become stronger, and more wrinkles appear.

2.2. Capillary Homogenization

Surface tension can also smooth or homogenize a solid shape if it has localized regions of high curvature. This is commonly seen when a soft gel is cast in a stiff mold having sharp edges and corners, with examples including the flattening of rough surfaces, smoothing of sharp corners, and shortening of long cylinders (48–50). With regard to the latter, Mora et al. (50) showed that a soft cylinder shrinks with stretch ratio λ , which depends on the elastocapillary number Σ (as shown in **Figure 3a**). In each of these cases, capillarity tends to minimize the surface area by removing regions of high curvature that would otherwise generate localized regions of high stress according to the Young–Laplace equation (see the reviews by Style et al. (15) and Bico et al. (12) for discussions on the pioneering works on the smoothing effects of solid surface tension). More recently, Hui et al. (52) have developed a generalized model for capillary flattening of an arbitrary elastic surface, showing that periodic surface structures are smoothed by surface tension without changing their period. Molefe & Kolinski (51) have shown that the shape of rectangular micropillars in a soft solid becomes rounded and is affected by the distance between neighboring structures, as shown in **Figure 3b**. This shows an application of the homogenizing behavior in soft solids that can be leveraged to shape a collection of structures for large-scale pattern formation. Sharp corners can also be formed by adhesive forces during the removal of an object from the interface of a

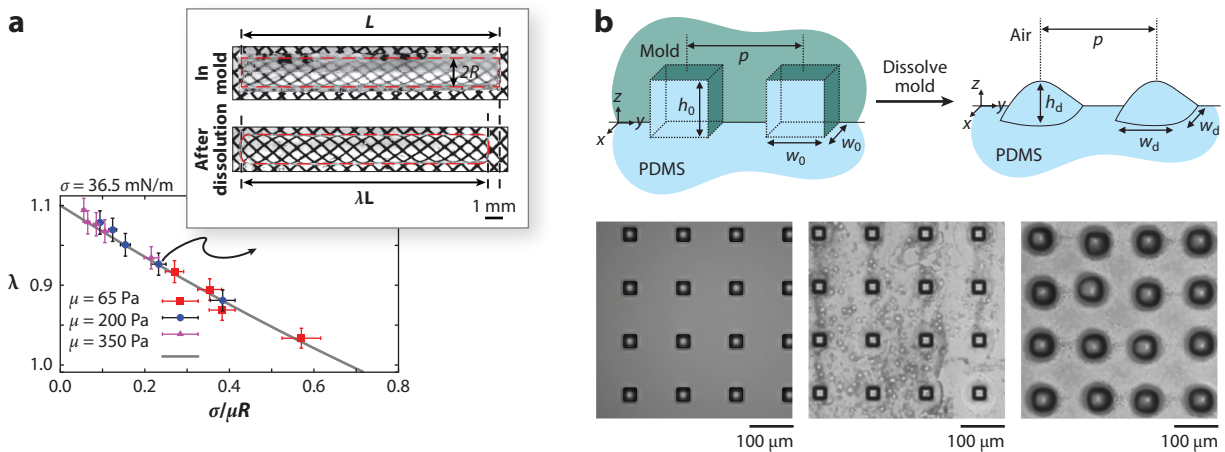


Figure 3

Capillary contraction and smoothing. (a) The length of a cylinder of agar gel immersed in toluene shortens due to capillarity, as defined by the axial stretch ratio λ plotted against the elastocapillary number $\Sigma = \sigma/\mu R$. (b) Micropatterned surface structures with sharp edges in PDMS gels become rounded by the presence of adjacent structures due to capillarity. Panel a adapted with permission from Reference 50; provided by S. Mora. Panel b adapted with permission from Reference 51; provided by J. Kolinski. Abbreviation: PDMS, polydimethylsiloxane.

soft polydimethylsiloxane (PDMS) substrate. Here, upon release of the extensional strain, surface tension is allowed to smooth out the corners, creating a rounded edge over a finite timescale that evolves in a self-similar manner (53).

3. DYNAMICS

Soft interfaces can reconfigure dynamically, resulting in the formation of oscillatory surface waves or irrecoverable deformation, i.e., instability, as discussed in the prior section. Whereas static (energy) stability analysis can determine if a base configuration is stable or unstable, dynamic stability analysis can provide information about the resulting pattern formation through identification of the dominant or fastest growing mode. The static stability limit can be recovered by setting the growth rate to zero. These two perspectives are complementary, and this is best illustrated from a historical perspective of the PRI (see the sidebar titled Plateau–Rayleigh Instability: A Historical Perspective). Soft solids differ from liquids in that both surface tension and elasticity resist deformation, and the timescale over which this deformation occurs depends on the material properties or rheology. In this section, we describe the interface dynamics of soft materials having

Rheology: the study of the flow of matter, both liquid and solid

PLATEAU–RAYLEIGH INSTABILITY: A HISTORICAL PERSPECTIVE

It has been known since the time of Plateau (1863) that a liquid cylinder will break up into droplets due to surface tension forces. Plateau was able to show using energy arguments (static stability) that liquid cylinders with length longer than the circumference are unstable, the well-known Plateau limit, but he incorrectly used this limit to predict the final drop size and spacing (wavelength). Some years later, Lord Rayleigh (in 1879) using a hydrodynamic approach calculated the instability growth rate, as it depends on the disturbance wave number (dynamic stability), which gave a good approximation to the final drop pattern. For good reason, the PRI bears both names as appropriate for their unique and complementary contributions to this problem.

viscoelasticity by framing the recent literature as analogous hydrodynamic instabilities with elastocapillary effects.

Consider the soft solid shown in **Figure 1**, with density ρ , complex modulus $\mu = \mu' + i\mu''$, and surface tension σ . Here, the material is defined on a domain D that is bound by a free interface ∂D^f and support surface ∂D^s . For a linear viscoelastic material, the stress \mathbf{T} and strain $\boldsymbol{\varepsilon}$ fields are related through the constitutive law,

$$\mathbf{T}(t) = 2 \int_{-\infty}^t \mu(t-t') \frac{\partial \boldsymbol{\varepsilon}(t')}{\partial t'} dt' + \mathbf{I} \int_{-\infty}^t \lambda(t-t') \frac{\partial (\text{Tr } \boldsymbol{\varepsilon}(t'))}{\partial t'} dt', \quad 5.$$

where μ and λ are the relaxation moduli, which are related to one another through the Poisson ratio ν : $\lambda = 2\nu\mu/(1-2\nu)$. Typical values for the rheological properties of μ and λ are provided by Barnes (54). The strain field is related to the displacement field \mathbf{U} through the relationship $\boldsymbol{\varepsilon} = (\nabla \mathbf{U} + \nabla \mathbf{U}^T)/2$. The governing boundary value problem is defined by the domain equation,

$$\nabla \cdot \mathbf{T} = \rho \frac{\partial^2 \mathbf{U}}{\partial t^2}, \quad 6.$$

with boundary conditions on the free surface ∂D^f and support surface ∂D^s :

$$\mathbf{n} \cdot \mathbf{T} \cdot \mathbf{n} = \sigma \mathcal{H}, \quad \mathbf{n} \cdot \mathbf{T} \cdot \mathbf{t} = 0 [\partial D^f]; \quad \mathbf{U} = \mathbf{0} [\partial D^s]. \quad 7.$$

On the free interface ∂D^f , stress continuity gives rise to (a) the Young–Laplace equation relating the normal stress difference across the interface to the curvature \mathcal{H} , there giving rise to elastocapillary effects, and (b) a shear-free condition. No displacement conditions are enforced on the support surface ∂D^s . The curvature is defined by the surface shape through the normal component of the interface displacement $\mathcal{H} = \mathcal{H}(\mathbf{U} \cdot \mathbf{n}|_{\partial D^f})$. We note that a spatially dependent surface stress would give rise to a Marangoni-like stress (as with liquids), but for the purposes of our discussion, we assume a uniform surface stress, i.e., surface tension.

It is often convenient to analyze the temporal viscoelastic material response in the frequency domain ω , and this is done by applying the Fourier transform $\tilde{f}(\omega) = \int_{-\infty}^{\infty} f(t) e^{i\omega t} dt$ to the governing equations,

$$(\tilde{\lambda}(\omega) + \tilde{\mu}(\omega)) \nabla (\nabla \cdot \mathbf{u}) + \tilde{\mu}(\omega) \nabla^2 \mathbf{u} = -\rho \omega^2 \mathbf{u}. \quad 8.$$

Here, we define the frequency-dependent complex modulus,

$$\tilde{\mu}(\omega) = i\omega \int_0^{\infty} \mu(t) e^{-i\omega t} dt, \quad 9.$$

which can be written as $\tilde{\mu}(\omega) = \mu'(\omega) + i\mu''(\omega)$, with $\mu'(\omega)$ being the storage modulus and $\mu''(\omega)$ being the loss modulus. The form of the complex modulus $\tilde{\mu}(\omega)$ depends on the rheology of the soft material (see the sidebar titled Rheology of Soft Polymer Gels). Two classical models of viscoelasticity relevant to soft polymeric materials are the (a) Kelvin–Voigt $\mu = \mu_0(1 + i\omega\tau_s)$ and (b) Maxwell $\mu = \mu_e \frac{i\omega\tau_f}{1+i\omega\tau_f}$ models. Both models are defined by a single viscoelastic timescale, τ_s and τ_f for Kelvin–Voigt and Maxwell, respectively. Here, τ_s represents the creep and τ_f represents the stress relaxation found in solid-like and liquid-like materials, respectively. We note that the Kelvin–Voigt model has nonzero shear modulus μ_0 at zero frequency and is, therefore, representative of solid-like materials such as gels, whereas the Maxwell model has zero loss modulus at high frequency and is more applicable to fluid-like materials, such as polymer solutions.

A solution of the governing equation can be facilitated through Helmholtz decomposition of the displacement field,

$$\mathbf{u} = \nabla \Phi + \nabla \times \mathbf{F}, \quad 10.$$

Viscoelasticity:

the time-dependent property of materials that exhibit both viscous and elastic characteristics when deformed

Helmholtz decomposition:

the representation of a vector field by decomposition into the sum of rotational and irrotational fields

RHEOLOGY OF SOFT POLYMER GELS

Polymer gels have a network structure of large molecular chains that are capable of inducing both elastic and viscous responses in a material when stressed. Cross-linking is responsible for the material elasticity and occurs at the gelation point or transition from liquid to solid-like behavior. Many of the studies of capillary solids discussed in this review utilize hydrogels, such as agarose and polyacrylamide, as the soft solid, primarily for their ability to tune the elasticity by varying the polymer concentration. The rheology, or material response, of polymer gels is characterized by the complex modulus $\mu = \mu' + i\mu''$ as measured using oscillatory shear tests in a rheometer. The most commonly used constitutive models of soft solids range from neo-Hookean models for nonlinear purely elastic materials to Kelvin–Voigt and Maxwell models for linear viscoelastic materials, with the distinction between the latter two types related to whether the material is characterized as a viscoelastic solid or viscoelastic liquid, respectively. More general models of viscoelasticity will need to be developed as designer gels are fabricated with desired material properties.

into scalar Φ and vector \mathbf{F} potentials, which when chosen properly result in a set of uncoupled Helmholtz equations from which the complex frequency $\omega = \omega_r + i\omega_i$ can be computed from the solvability condition associated with the boundary conditions. Here, stability is determined by the sign of ω_i , with $\omega_i > 0$ giving stability (i.e., damped oscillations) and $\omega_i < 0$ giving instability with corresponding growth rate $s = -\omega_i$.

3.1. Pattern Formation

The fundamental ansatz in dynamic linear stability analysis is that the material is subject to an arbitrary spatial disturbance that can be represented as a Fourier series with components defined by a wavelength λ or, equivalently, wave number $k \equiv 2\pi/\lambda$. Each Fourier component has an associated growth rate, and the surface pattern that develops is associated with the Fourier mode having the largest growth rate. This can be either instability driven or a resonant phenomena, and we discuss both in what follows. Whenever the spatial wavelength is small relative to the characteristic length scale of the domain L (or container geometry), $\lambda \ll L$, then the domain can be considered semi-infinite and a classical dispersion relationship $\omega = \omega(k)$ is obtained, with continuous wave number k and corresponding zero bandwidth. In contrast, when $\lambda \approx L$, the surface pattern conforms to the container geometry, is described by a discrete mode number pair, and has a finite bandwidth over which that particular mode can be excited. In this case, the boundary conditions at the solid support affect the frequency ω , whereas in the former they play no role.

3.2. Dimensionless Groups

Surface pattern formation can be complex because soft polymeric materials often exhibit a complex rheology characterized by both elasticity and viscosity, making this an inherent multiphysics problem. To better understand the physics and relevant limiting cases, one can nondimensionalize the governing equations and resulting dispersion relationships, which gives rise to a set of dimensionless numbers that define such systems. Here, the relevant timescales are the capillary timescale $t_c = \sqrt{\rho L^3/\sigma}$, elastic timescale $t_e = \sqrt{\rho L^2/\mu_0}$, viscous timescale $t_v = \gamma L/\sigma$ with γ the viscosity, and viscoelastic relaxation time τ (55). The relative balance of these timescales gives rise to a set of dimensionless parameters that define the physics. Here, the elastocapillary number appears naturally as the ratio of capillary and elastic timescales $\Sigma \equiv t_c/t_e = \sigma/L\mu_0$. The compressibility number can be defined as the ratio of compressional to shear wave speeds $\kappa \equiv \mu/(\lambda + 2\mu) = \sqrt{(1-2\nu)/(1+\nu)}$. The Ohnesorge number $Oh \equiv t_v/t_c = \gamma/\sqrt{\rho\sigma L}$ is a balance of viscosity and capillarity.

Deborah number:

a dimensionless number $\zeta \equiv \tau_r/t_c$ relating the material relaxation time τ_r to a characteristic timescale t_c to characterize a material's fluidity

Bond number:

a dimensionless number $B_0 = \rho g L^2 / \sigma$ used to characterize the relative importance of gravitational to surface tension effects at a liquid interface

Dispersion

relationship: a functional relationship between the frequency ω and wave number k , $\omega = \omega(k)$

Viscoelastic effects are slightly more nuanced, and one typically defines the Deborah number depending upon if the material is more solid-like (Kelvin–Voigt) or fluid-like (Maxwell). For a Kelvin–Voigt solid, one can define the solid Deborah number $\zeta_s \equiv \tau_s/t_e = \tau_s \sqrt{\mu_0/\rho L^2}$ with limiting cases corresponding to $\zeta_s = 0$, the purely elastic limit, and $\zeta_s = \infty$, the purely viscous limit. For a Maxwell fluid, the fluid Deborah number $\zeta_f \equiv \tau_f/t_c = \tau_f \sqrt{\sigma/\rho L^3}$, from which $\zeta_f = 0$ corresponds to viscous fluids and $\zeta_f = \infty$ corresponds to purely elastic solids. The special case $\zeta_f > 1 > Ob$ ($\tau_f > t_c > t_v$) corresponds to an inviscid elastic fluid (56), which is typical of dilute polymer concentrations, such as those typically used in bioinks (57, 58). Whenever an external force is present in the system, such as gravity, an additional dimensionless number can be defined relative to the chosen timescale, e.g., for gravity the elastogravity number $\alpha = \rho g L / \mu_0$ or Bond number $B_0 = \rho g L^2 / \sigma$. Lastly, whenever the domain is of finite size, then an aspect ratio $\Lambda = L_x/L_y$ can be defined, e.g., the slenderness of a cylinder $\Lambda = R/L$.

3.3. Elastocapillary-Gravity Waves

Free surface waves travel on a semi-infinite material with dispersion relationship $\omega(k)$. For a pure elastic solid, Rayleigh (59) showed that the dimensionless wave frequency $\beta = \rho \omega^2 / \mu k^2$ is determined from the following characteristic equation:

$$\beta^3 - 8\beta^2 + 8\beta(3 - 2\kappa) - 16(1 - \kappa) = 0. \quad 11.$$

For incompressible materials $\kappa \rightarrow 0$, Equation 11 admits the Rayleigh wave dispersion relationship,

$$\omega = 0.955 \sqrt{\frac{\mu}{\rho}} k, \quad 12.$$

which shows pure elastic waves are nondispersive and propagate with a constant wave speed $c = \omega/k$ that scales as $c \sim \sqrt{\mu/\rho}$. In contrast, for a pure liquid the waves formed are capillary-gravity waves with dispersion relationship (60),

$$\omega = \sqrt{gk + \frac{\sigma}{\rho} k^3}. \quad 13.$$

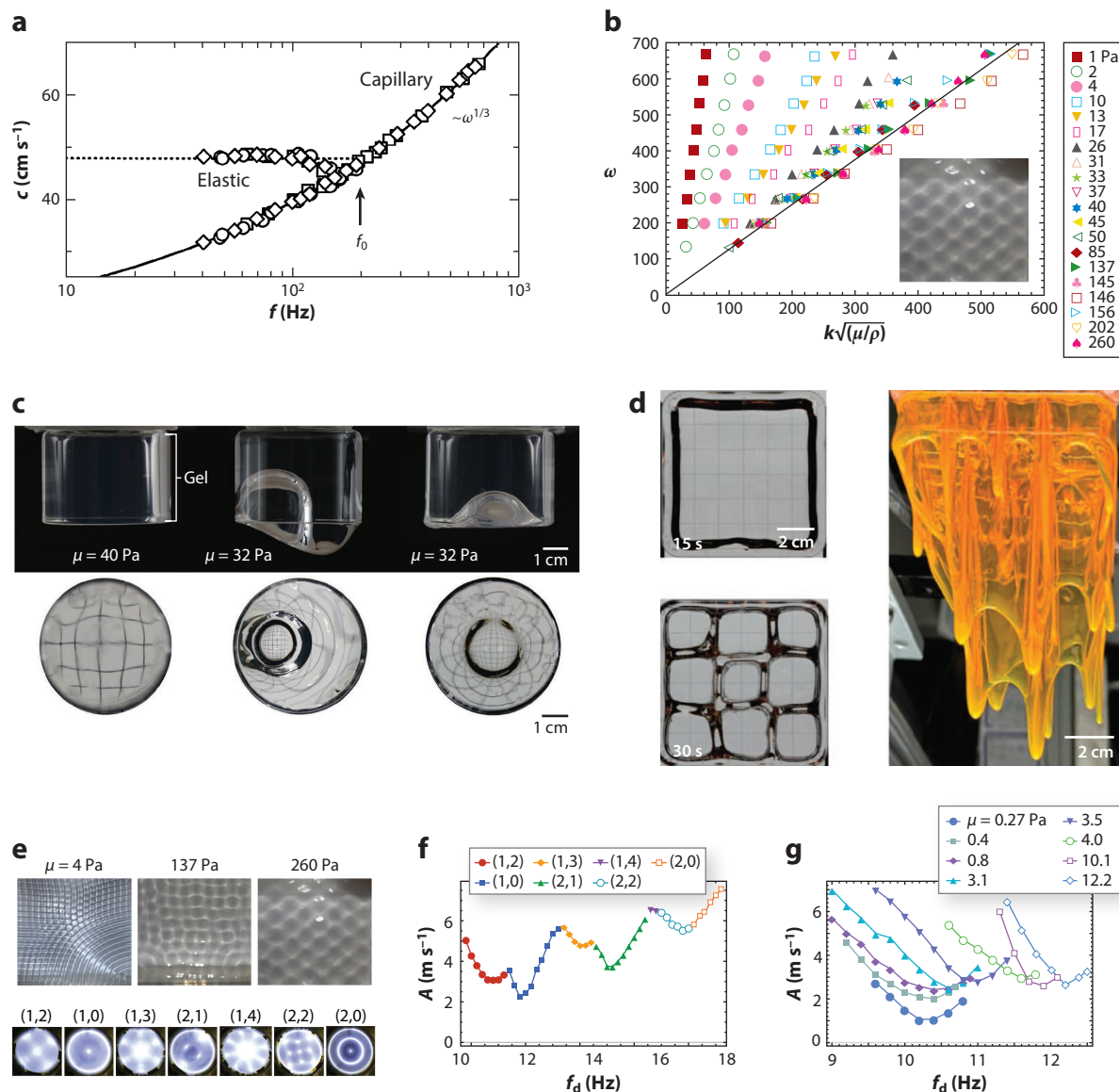
Here, gravity is introduced into the problem through the normal stress boundary condition, Equation 7, as an excess hydrostatic pressure due to the interface deflection from the base state. Unlike elastic Rayleigh waves, capillary-gravity waves are dispersive with a wave speed that depends on the wave number k ; the speed of gravity waves $c \sim k^{-1/2}$ decreases with wave number, while the speed of capillary waves $c \sim k^{1/2}$ increases with wave number. For soft viscoelastic materials, one should expect the dispersion relationship to encompass both Rayleigh waves and capillary-gravity waves in what is referred to as elastocapillary-gravity waves.

Harden, Pleiner & Pincus (61) put forth the first model of surface waves on a viscoelastic material using a hydrodynamic theory of polymeric liquids. The dispersion relationship is given by

$$(i\omega + 2\nu(\omega)k^2)^2 - 4\nu(\omega)^2 k^4 \left(1 + \frac{i\omega}{\nu(\omega)k^2}\right)^{1/2} + \frac{\sigma k^3}{\rho} = 0, \quad 14.$$

where $\nu(\omega)$ is the complex kinematic viscosity defined by $\nu(\omega) = \nu^*(\omega) + \mu(\omega)/i\omega$, with $\nu^*(\omega)$ and $\mu(\omega)$ being the frequency-dependent viscosity and shear modulus, respectively. Their model predicts capillary waves ($\omega \sim k^{3/2}$) at the surface tension-dominated limit and Rayleigh waves ($\omega \sim k$) at the elasticity-dominated limit, as well as overdamped nonpropagating waves ($\omega \sim ik$) at

the viscosity-dominated limit. A similar approach has been taken by Onodera & Choi (62), who formulate their model using an elasticity theory. The hydrodynamic and elasticity approaches yield similar results. These theoretical predictions were corroborated by the seminal experiments of Monroy & Langevin (63), who studied electrically excited traveling waves on agarose gel (shown in **Figure 4a**, which plots the wave speed c against the frequency f). In addition to observing crossover behavior at frequency f_0 between elastic waves and capillary waves with increasing wave number k , they also observed modal coexistence of a propagating Rayleigh wave and propagating capillary-gravity wave for a single driving frequency in the crossover region. The review article by Monroy (68) provides a very detailed discussion and historical perspective of this important problem in



(Caption appears on following page)

Figure 4 (Figure appears on preceding page)

Elastocapillary-gravity waves. (a) Traveling wave speed c against frequency f (Hz) on a soft gel substrate reveals capillary waves above and the combination of capillary waves and elastic waves below the elastocapillary transition frequency f_0 . (b) Standing wave frequency ω against scaled wave number $k\sqrt{\mu/\rho}$ shows a collapse of the data for elastic waves and noncollapse highlighting capillary effects on the dispersion relationship. (c) A cylindrical container filled with a soft gel is turned upside down and subject to the buoyancy-driven Rayleigh–Taylor instability. The surface remains flat for $\mu = 40$ Pa but can exhibit one of two unique surface patterns when $\mu = 32$ Pa, the (1,0) and (1,1) modes. (d) Viscoelasticity affects the Rayleigh–Taylor instability of a soft PDMS gel with large relaxation time in a rectangular container. (e) Faraday waves appear on the surface of a gel in a mechanically vibrated container and exhibit a subharmonic response such that the wave frequency f is half the driving frequency f_d , $f = f_d/2$. The corresponding surface wave pattern is characterized by a continuous wavelength λ for large containers (*top*) and conforms to the container geometry for small containers (*bottom*), and is described by a discrete mode number pair (n, ℓ) for the cylindrical container shown here. (f) A frequency sweep plotting acceleration A against driving frequency f_d reveals an instability tongue for each mode (n, ℓ) , above which one observes that wave pattern. (g) The shape of the instability tongue, e.g., for the (1,2) mode, depends on the shear modulus μ . Panel *a* adapted with permission from Reference 63; provided by F. Monroy. Panel *b* adapted from Reference 64 with permission from the Royal Society of Chemistry. Panel *c* adapted with permission from Reference 65; provided by S. Cai. Panel *d* adapted with permission from Reference 66; copyright 2023 American Chemical Society and provided by J. Nunes and H. Stone. Panel *e* adapted from Reference 64, with permission from the Royal Society of Chemistry, and with permission from Reference 67, copyright 2020 American Physical Society. Panels *f* and *g* adapted with permission from Reference 67; copyright 2020 American Physical Society. Abbreviation: PDMS, polydimethylsiloxane.

the field of elastocapillarity. More recently, Shao et al. (64) have studied standing elastocapillary-gravity waves on mechanically vibrated agarose gels in a regime where the elastocapillary $\ell_c = \sigma/\mu$ and elastogravity $\ell_g = \mu/\rho g$ lengths are of similar magnitude $\ell_c, \ell_g \sim 0.01 - 1$ cm, as shown in **Figure 4b**, which plots the wave frequency ω against Rayleigh wave frequency $k\sqrt{\mu/\rho}$ for a range of shear modulus $1 < \mu < 260$ Pa showing where capillarity is important. Further experiments by Chantelot et al. (69) on the same material studied the effect of thickness of the gel substrate, which enters the problem as an additional length scale b and is important whenever it is similar in size to ℓ_c and/or ℓ_g .

Elastocapillary-gravity waves in small containers conform to the container geometry, as shown in the experiments by Shao et al. (70, 71) in mechanically excited cylindrical containers. Here, the spatial structure of the wave is essentially described by a Bessel function $J_\ell(k_{n\ell}r)$ defined by the mode number pair (n, ℓ) . For small containers, the boundary conditions at the contact line on the container sidewall become important, and one often creates (a) pinned or (b) freely sliding conditions in experiment, and this affects the wave frequency. Wilson et al. (72) have derived a dispersion relationship,

$$\lambda_{n\ell} \equiv \omega\sqrt{\rho R^3/\sigma} = i\text{Oh}k_{n\ell}^2 \pm \sqrt{(\text{Bo}k_{n\ell} + k_{n\ell}^3) \tanh(k_{n\ell}b) + 2k_{n\ell}^2 \frac{1}{\Sigma} - \text{Oh}^2 k_{n\ell}^4}, \quad 15.$$

using the modeling approach of Harden et al. (61) but adapted for the case of a material in a cylindrical container with constant viscosity and constant elasticity and freely sliding contact line. Here, $k_{n\ell}$ is the n th zero of $J_\ell(k)$, $\text{Bo} = \rho g R^2/\sigma$ is the Bond number, and $b = H/R$ is the container aspect ratio. For pinned contact-line conditions, the analysis is slightly more involved, and a Rayleigh–Ritz variational procedure is invoked over a constrained function space, precluding a closed form dispersion relationship for this case. This model agrees well with a wide range of experimental observations.

3.3.1. Rayleigh–Taylor instability. For the elastocapillary-gravity waves discussed above, gravity is typically oriented such that the denser medium (gel) is located below the lighter medium (air), giving rise to a stable configuration in which surface waves can only be generated through external forcing. If the configuration is flipped, i.e., the denser medium lies above the lighter medium, the interface is susceptible to the buoyancy-driven Rayleigh–Taylor instability (RTI) (73, 74). This is readily seen by examining Equation 13 for $g < 0$ and $\sigma = 0$, which gives rise to an imaginary

frequency $\omega \sim i\sqrt{gk}$, which corresponds to an exponential growth rate. Here, surface tension stabilizes higher wave numbers. For a pure liquid, the interface is always unstable to RTI and appears in fields such as astrophysics and turbulent mixing, as described in the review by Sharp (75). For soft solids, the elastic resistance can stabilize the RTI provided the elasticity is greater than some threshold value. This was clearly demonstrated in the experiments by Mora et al. (76), who observed the destabilization of polyacrylamide gels in upside-down cylindrical containers above a critical elastogravity number $\alpha = \rho gb/\mu > 6.22$, where b is the depth of the gel. Here, the interface can adopt a number of patterns, which is determined by pattern selection of a dominant mode shape that conforms to the cylindrical container. In certain parameter regimes, two dominant modes may coexist as demonstrated in the experiments by Zheng et al. (65) and shown in **Figure 4c**, where the (1, 0) and (1, 1) modes are observed for the same experimental conditions. In general, there usually exists a number of unstable modes, and the one that is ultimately observed is the one with the fastest growth rate, as determined by dynamic stability analysis, which has been performed for the RTI of a soft viscoelastic material by Tamim & Bostwick (77). They document the dominant instability mode, as it depends on the relevant dimensionless parameters, showing how the container geometry plays a key role in the pattern formation, which agrees well with experimental observations (65). Slutzky et al. (66) have experimentally studied RTI in cross-linked PDMS in a rectangular channel with $\mu_0 \sim O(1 \text{ Pa})$ and high relaxation times $\tau \sim O(10 \text{ s})$ to illustrate the combined effect of viscoelasticity and surface tension on the pattern formation (cf. **Figure 4d**). In particular, they show that viscous dissipation in the solid during growth of the primary instability can lead to intricate secondary buckling patterns. Outside of gels, RTI has similarly been observed in elastic and elastoplastic materials with relevance to high energy density physics (78–81). More recent work on RTI has considered additional effects such as convergent geometry and centrifugal forces, paving the way for utilizing this mechanism in the design of soft solids (82, 83).

3.3.2. Dynamics of Plateau–Rayleigh instability in viscoelastic solids. The method of dynamic stability analysis has also been applied to PRL, in a similar manner to that of Rayleigh’s contribution to the original fluid instability. Tamim & Bostwick (84) have derived dispersion relations that predict the growth rate of unstable modes in linear soft viscoelastic solid and hollow cylinders, which recover the static stability limit for the solid cylinder $\Sigma_c = 6$ and hollow cylinder $\Sigma_c = 2$. Using a power-law rheological model applicable to cross-linking polymers, they showed a decrease in the dominant wave number with increased elasticity and viscous dissipation in both cases. Pandey et al. (85) have studied the dynamic mode selection in neo-Hookean elastic threads under a slender-body approximation and showed that the fastest growing wave number determines the nonlinear states such as the beads-on-a-string or cylinders-on-a-string structure.

3.4. Parametric Waves

Parametric oscillations occur in systems in which one of the governing parameters exhibits temporal periodicity and often leads to a threshold instability when the system is driven beyond a critical parameter value. This was observed experimentally for capillary-gravity waves on a vertically vibrated fluid bath by Faraday (86), who observed a subharmonic wave response in which the wave oscillates at half the driving frequency, $\omega = \omega_d/2$. These are more commonly referred to as Faraday waves, which have become synonymous with pattern formation on interfaces (see the sidebar titled Patterning Surfaces by Mechanical Vibration). For reference, we refer the reader to the review by Miles & Henderson (94) on Faraday waves in Newtonian fluids with a focus on geometric confinement and nonlinear modal interactions.

PATTERNING SURFACES BY MECHANICAL VIBRATION

It has been known since the time of Faraday (1831) (86) that a standing wave pattern can be formed at the free surface of a mechanically vibrated container filled with fluid, hereafter referred to as Faraday waves. At that time, there was some dispute regarding the temporal wave response, with Faraday (86) reporting waves that oscillate at half the driving frequency (subharmonic response), whereas Matthiessen (87) reported waves that oscillate at the driving frequency (harmonic response). Lord Rayleigh (88) conducted experiments that supported Faraday's observations. This dispute was resolved by the theoretical analysis put forward by Benjamin & Ursell (89), who showed that the wave amplitude obeyed a Mathieu equation with a solution that supported both sets of observations. Since that time, Faraday waves have become synonymous with pattern formation and have been used to study nonlinear and emergent phenomena in fluids, including the redistribution of particles (90) and surfactants (91) on thin liquid films, and the rearrangement of layers of granular materials (92) and to induce turbulent mixing of two miscible fluids (93). Recent interest in tissue engineering has motivated the use of Faraday waves to control the assembly of organoid cells in bioprinting technologies, where the working material is a soft hydrogel (6). Experiments by Shao et al. (64, 67) highlight the role of solid surface tension on Faraday waves in soft gels.

The classical modeling approach for Faraday waves is attributed to Benjamin & Ursell (89) and involves introducing a time-dependent gravitational acceleration $g(t) = g - A \cos(\omega_d t)$, with A being the driving acceleration, into the governing Equations 6 as a body force $\mathbf{F} = \rho g(t)\hat{z}$. This gives rise to a set of Mathieu equations for the respective surface wave modes x ,

$$\ddot{x} + c\dot{x} + (p - A \cos(\omega_d t))x = 0, \quad 16.$$

where $p = \omega_0^2$ is related to the natural frequency ω_0 for the system, and the damping constant c incorporates various forms of dissipation in the system, such as viscous dissipation or contact-line dissipation in systems with moving contact lines. Standing waves appear as solutions of the Mathieu equation (Equation 16) in regions of the driving frequency–amplitude ω_d – A parameter space defined by the tongues-of-instability for subharmonic, harmonic, and superharmonic temporal responses, respectively. Floquet theory is often used to determine the shape of the tongues (95). Damping shifts the tongues to higher accelerations, leading to a nontrivial threshold acceleration A_c . For most pure liquid systems, the subharmonic tongue has the lowest threshold acceleration A_c and, for this reason, are most readily observed experimentally. However, there are exceptions for thin viscous liquid layers in which the harmonic instability tongue has shifted lower than the subharmonic tongue (96). Viscoelastic effects in polymeric liquids can significantly alter the Faraday wave properties by modifying the threshold acceleration for surface waves (97, 98). Harmonic waves are the dominant instability mode for a Maxwell model fluid when elastic effects control the material response (99, 100).

Faraday waves have been recently observed by Shao et al. on agarose gels in large containers (64) and small cylindrical containers (67). These surface waves exhibit a subharmonic temporal response with continuous spatial wave number for large containers (cf. **Figure 4e, top**), but conforms to the container geometry for small containers (cf. **Figure 4e, bottom**) and are defined by the mode number (n, ℓ) discussed above. **Figure 4f** shows the instability tongues for an ultrasoft gel in a small cylindrical container by plotting the driving acceleration A against the driving frequency f_d . Note that some modes are accessible over only a small frequency range, highlighting modal competition in the emergent pattern formation behavior. For a fixed mode $(1, 2)$, **Figure 4g** shows how the instability tongues shift toward higher resonance frequency and threshold acceleration with increasing shear modulus, thus highlighting the role of elastocapillarity. Theoretical

Tongues-of-instability: regions of parameter space for the Mathieu equation where a given system response—subharmonic, harmonic, and superharmonic—is observed

analysis by Bevilacqua et al. (101) for a semi-infinite slab of neo-Hookean material shows how pattern formation critically depends on the elastocapillary number, with highly elastic materials favoring harmonic waves over those of subharmonic ones. For low driving frequency, their analysis recovers the stability limit for the elastic RTI reported by Mora et al. (76).

3.5. Drop Oscillations

It has been known since the time of Lord Rayleigh (1879) (28) that an inviscid liquid drop oscillates about its spherical equilibrium shape, reflecting a balance between inertia and capillarity, with characteristic frequency given by

$$\omega_\sigma^2 = \frac{n(n+2)(n-1)\sigma}{\rho R^3}, \quad 17.$$

with n being the polar wave number. This corresponds to the $\Sigma = \infty$ limit with the dynamics well established for Newtonian fluids (102–104) having been verified experimentally under terrestrial (105) and microgravity (106) conditions, respectively. In contrast, the elastic limit $\Sigma = 0$ corresponding to the spheroidal oscillations of a linear elastic sphere has been established by Lamb (107–110), with frequency given by

$$\omega_\mu^2 = C(n) \frac{\mu}{\rho R^2}. \quad 18.$$

Here, the constant $C(n)$ must be determined numerically from a transcendental equation that arises from a solvability condition.

Shao et al. (111) have studied the oscillations of agarose gel drops in ultrasonic levitation focusing on the fundamental $n = 2$ oblate/prolate mode. By amplitude modulating the carrier wave field, shape oscillations were excited and frequency response diagrams, such as those shown in **Figure 5a**, were obtained through a frequency sweep with the natural frequency corresponding to that at the resonance peak. They performed experiments over a wide range of elastocapillary numbers Σ capturing the transition from capillarity-dominated to elasticity-dominated motions, as shown in **Figure 5b**, which plots the scaled frequency ω/ω_σ against Σ . To better understand

Ultrasonic levitation: an experimental technique for suspending materials in air using acoustic radiation pressure, which has been useful for creating containerless conditions

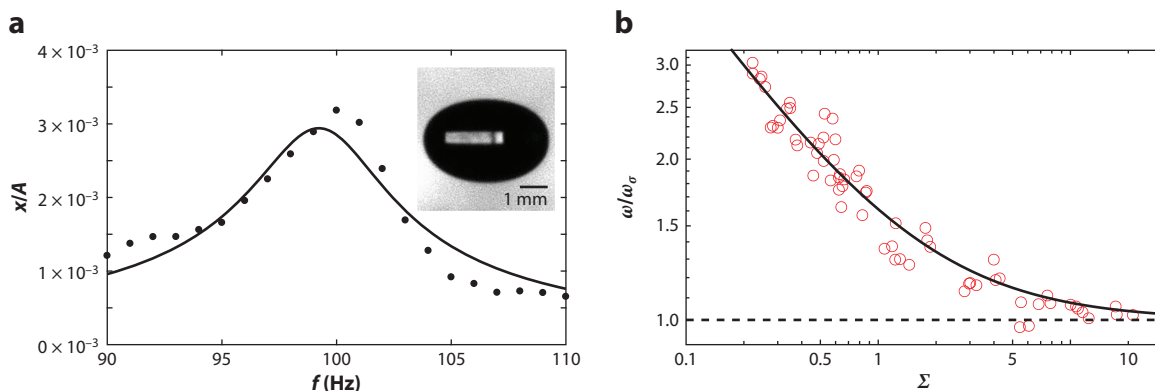


Figure 5

Oscillating gel drop in ultrasonic levitation has (a) a frequency response diagram with a single maximum associated with the resonance frequency for the fundamental $n = 2$ mode. (b) The scaled resonance frequency ω/ω_σ (with ω_σ being the capillary frequency) plotted against the elastocapillary number $\Sigma \equiv \sigma/GR$ reveals the elastocapillary transition from elastic wave behavior (*dot-dashed line*) $\Sigma \rightarrow 0$ to capillary wave behavior (*dashed line*) $\Sigma \rightarrow \infty$. Figure adapted with permission from Reference 111; copyright 2019 American Physical Society.

the elastocapillary transition, they introduce a low-order model in which surface tension and elasticity can be idealized as springs in parallel that admits an effective natural frequency for the drop,

$$\frac{\omega}{\omega_\sigma} = \sqrt{1 + \left(\frac{C}{8}\right) \frac{1}{\Sigma}}. \quad 19.$$

The best-fit parameter value $C = 12.75$ to the experimental data is slightly greater than that predicted by existing elastic theories $C = 7.1$, $C = 10$ (110, 112) number. The crossover region is determined by setting $\omega_\sigma^2 = \omega_\mu^2$ and gives rise to a critical elastocapillary number $\Sigma_c = 1.59$.

Sessile drops differ from free drops through their wetting interactions with the solid substrate, and there is no analogous closed-form dispersion relationship to Equation 17, even for inviscid sessile drops. However, Steen et al. (113) have revealed the complexity of the frequency spectrum for liquid sessile drops and organize the associated motions into a droplet motion periodic table (DMPT), documenting features such as spectral splitting and spectral reordering. Chakrabarti & Chaudhury (114) study the oscillations of sessile drops made of polyacrylamide gels, which are excited by white noise. Here, the resonant frequency is identified by peaks in the power spectrum. They scale their experimental data using a modified capillary frequency, which is necessary to account for the wetting properties, and show that their data collapse with a dispersion relationship nearly identical to Equation 19.

3.6. Drop Vibration Rheometer

There is a long history of using the oscillations of levitated drops for measuring fluid properties, as the procedure eliminates wetting effects making it a containerless process (115–119). Shao et al. (120) have used this approach to measure the surface tension and viscosity of a soft agarose gel drop, which is something that has been notoriously difficult to measure. We summarize the approach, which is based on lumped-parameter modeling and exploits the similarity of drop oscillations with the damped driven oscillator (121, 122),

$$\ddot{x} + 2\zeta\omega_n\dot{x} + \omega_n^2x = A \cos \omega t, \quad 20.$$

with ζ being the damping ratio, ω_n is the natural frequency, and (A, ω) are the driving amplitude and frequency, respectively. The steady-state frequency response of Equation 20 is given by

$$\frac{x}{A} = \frac{1}{\sqrt{\left(1 - \left(\frac{\omega}{\omega_n}\right)^2\right)^2 + \left(2\zeta\left(\frac{\omega}{\omega_n}\right)\right)^2}}, \quad 21.$$

which can be fit to experimental data $(x/A, \omega)$ to obtain ω_n and ζ , from which surface tension σ and viscosity μ can be inferred from models that define the spring constant and dashpot constants in terms of the material parameters. For an agarose gel drop, the normalized spring constant that incorporates elasticity and capillarity is given by Equation 19, whereas the damping ratio can be determined by evaluating the viscous dissipation, as computed by Lamb (60) and given by

$$\zeta = \frac{5\mu}{\rho R^2 \omega_n}. \quad 22.$$

There are limitations to this approach, which restricts to Newtonian materials whose elasticity and surface tension are uncoupled.

More sophisticated models of soft drop oscillations have been put forth by Tamim & Bostwick for a purely elastic drop (123) and viscoelastic drop with arbitrary rheology, including Kelvin–Voigt or Maxwell models (124), which are based on a solution of the field equations for a linear

viscoelastic material. This approach admits two types of solutions, (a) spheroidal modes (i.e., shape-change modes) and (b) torsional (rotational) modes, the latter of which are unaffected by elastocapillarity. For the spheroidal modes with fixed polar mode number n , there exists an infinity of radial motions defined by a radial mode number, each of which exhibits an elastocapillary transition that is accompanied by a qualitative change in the deformation field whereby a layer of recirculation vortices develop at the free surface. Viscoelastic effects give rise to complex frequencies characterized by an oscillation frequency and decay rate. Lastly, they predict a breathing mode instability for compressible drops, similar to that seen for bubbles in which surface tension overcomes the material resistance leading to droplet collapse, which appears in a region of the Σ and κ parameter space.

Spheroidal modes: characteristic frequency and mode shapes given by the spherical harmonic functions Y_n^m where n and m are polar and azimuthal mode numbers, respectively

4. CONCLUDING REMARKS

Soft solids are shaped by capillarity on scales less than the elastocapillary length, which is responsible for a number of beautiful and perhaps unexpected phenomena whose literature we have reviewed here. The resulting shape morphologies are either in equilibrium or have a pattern that evolves dynamically and, as such, can be broadly categorized into static and dynamic phenomena.

The two-phase soft solid systems discussed here can be accurately modeled by a constant surface tension. However, a more general description of surface stress with well-defined surface elastic constants may be required when the material is subjected to an external strain. One way to determine the strain-dependent surface response in soft solids is through the external stretch induced by a liquid droplet on a soft substrate, i.e., a three-phase system (17, 18), but here the experimental measurement is complicated by the stress singularity at the contact line (19, 125, 126). One proposed solution is to measure surface stresses in two-phase systems by inducing strains through alternative means (127, 128). Bain et al. (127) experimentally studied the surface stress through the free surface topography of PDMS gels, cured in a mold and then exposed to an applied external strain, to demonstrate the Shuttleworth effect. Although this technique for characterizing the solid surface stress using a two-phase system is more promising than a three-phase system, it still needs to be compared against different testing protocols. For example, Carbonaro et al. (128) have shown that spinning polyacrylamide hydrogels behave like a neo-Hookean material with constant surface tension. To address such issues associated with surface stress, a robust theoretical framework should be developed that can unify the different strain conditions and account for hyperelastic material response at large deformations (129, 130).

Nonlinear material response is readily seen in soft solids where, for example, strain stiffening can affect pattern formation (131, 132). This will become more important as novel soft materials are designed with desired characteristics like biocompatibility that necessitate a decoupling of elastic and viscous behavior in highly deformed states, as is relevant to novel noncontact rheological measurements (133, 134). Nonlinearity also appears through finite amplitude deformations that arise from instabilities, such as PRI or RTI, and lead to secondary stable states that are unique to soft solids (135). Models that include nonlinearity due to the aforementioned effects should be developed.

Surface tension in liquids is responsible for a broader range of hydrodynamic phenomena that has yet to be explored in soft solids (136). For example, surface tension gradients give rise to the well-known Marangoni effect that drives interfacial flows responsible for, e.g., tears of wine (137, 138). The Marangoni effect in solids may explain cell aggregation and tissue migration during biological processes such as morphogenesis and wound healing (139, 140). The introduction of surface tension in mechanical models of soft solids can also provide insights into a variety of

biological processes such as the patterning of damaged axons (141) and muscle contraction during inhalation (142). From an engineering design perspective, there is great potential for soft structural prototypes in which surface tension can induce active shape changes when driven out of equilibrium (143, 144). Lastly, recent studies of capillarity in solids and solid-like materials (e.g., yield stress fluids) have given rise to new areas of research such as plastocapillarity (145) and poroelastocapillarity (146) that should be explored further.

SUMMARY POINTS

1. Self-capillarity in solids arises from the free surface energy and becomes important on length scales L that are smaller than the elastocapillary length $\ell_e = \sigma/\mu$. For soft solids, such as hydrogels, ℓ_e can be millimetric with solid capillarity responsible for many new and unexpected results. For both static and dynamic phenomena, the elastocapillary number $\Sigma \equiv \ell_e/L = \sigma/\mu L$ helps define a transition Σ_c between elasticity-dominated $\Sigma < \Sigma_c$ and capillary-dominated $\Sigma > \Sigma_c$ material response.
2. Surface tension affects the static equilibrium shape of soft solids, as defined relative to rigid solids, through rounding of sharp corners and inducing shape-change morphologies, such as pearling, creasing, and wrinkling. These unique shapes result from a competition between the elastic energy cost due to deformation and the gain in surface energy due to shape change.
3. The regularization of the Biot instability of a uniaxial compressed solid by surface tension is responsible for predicting a dominant wavelength for the wrinkling patterns that has been validated experimentally, thus helping resolve a historical paradox.
4. A number of pattern formation phenomena have been recently observed in soft solids that are analogous to classical hydrodynamic interfacial instabilities, such as the Rayleigh–Taylor instability, the Plateau–Rayleigh instability, elastocapillary-gravity waves, Faraday waves, and drop oscillations, but whose stability properties depend on elasticity through a number of new dimensionless numbers. The resulting patterns can be identified through dynamic stability analysis by identification of the dominant spatial mode with maximum growth rate.
5. Polymeric soft gels often exhibit nontrivial viscoelastic behavior that affects the dynamics of soft solids, as defined by the Deborah number ζ .
6. The wave dynamics in soft solids can be used as a nondestructive diagnostic technique to measure the surface tension of soft solids, which has been notoriously challenging, as well as other material properties such as viscosity and elasticity. This technique has been applied to planar surface waves and acoustically levitated drops, with the latter being notable as a containerless process.

FUTURE ISSUES

1. Future theoretical models should include nonlinear constitutive laws for hyperelastic materials, as required to generalize the Shuttleworth effect and compare with relevant experiments for large deformations.

2. Interfacial instabilities, such as Plateau–Rayleigh instability and Rayleigh–Taylor instability (RTI), in soft solids have well-defined stability thresholds with pattern formation determined by mode selection of the primary instability. However, secondary instabilities have been observed as bifurcations from the primary instability branch, e.g., for RTI, when the size of the deformation becomes large enough to induce nonlinear effects. Large deformation models should be developed so as to better understand how to access and harness these secondary instabilities.
3. Pattern formation in soft solids is affected by container geometry (or confinement), but it is not well known what the role of the physics at the soft solid–container interface plays in that process, either experimentally or theoretically. Here, adhesion or frictional effects will couple with elastocapillary effects at the free surface to give rise to potentially new multiphysics phenomena.
4. Surface stress gradients can give rise to a Marangoni effect in solids that has shown to be responsible for cell migration through durotaxis and mechanotaxis but could also be used for surface patterning of soft solids that could be guided by our understanding of analogous hydrodynamic flows, e.g., Rayleigh–Benard–Marangoni convection. Such gradients could be generated by mechanics, chemistry, biology, or active soft matter.
5. Much of the existing literature has been fundamental, but there exists a lot of potential in applied areas in which self-capillarity is relevant, including biology, tribology, and nanotechnology.
6. Advances in polymer chemistry have allowed for the fabrication of designer polymer gels with prescribed rheology. Models must be developed for arbitrary rheology so as to better predict and control surface patterns for, e.g., manufacturing processes that involve soft materials.
7. Self-capillarity in soft materials with a more complex rheology has given rise to the new fields of plastocapillarity (yield stress materials) and poroelastocapillarity (poroelastic materials), which are in their infancy and should be explored further.

DISCLOSURE STATEMENT

The authors are not aware of any affiliations, memberships, funding, or financial holdings that might be perceived as affecting the objectivity of this review.

ACKNOWLEDGMENTS

We thank J. Kolinski, S. Karpitscka, J. Snoeijer, J. Nunes, H. Stone, F. Monroy, S. Cai, and S. Mora for supplying some of the experimental graphics used in this review. We would like to thank S. Mora for useful discussions in framing the content of this manuscript. We acknowledge C. Gabbard for assistance with the graphics. J.B.B. acknowledges support from NSF grant CBET-1750208.

LITERATURE CITED

1. Ahmed HE, Salman B, Kherbeet AS, Ahmed M. 2018. *Int. J. Heat Mass Transfer* 118:129–53
2. Han JC. 2013. *J. Therm. Sci. Eng. Appl.* 5(2):021007
3. Bayer SA, Altman J. 2005. *The Human Brain During the Second Trimester*. Boca Raton, FL: CRC
4. Castellucci M, Schepe M, Scheffen I, Celona A, Kaufmann P. 1990. *Anat. Embryol.* 181:117–28

5. Chen P, Luo Z, Güven S, Tasoglu S, Ganesan AV, et al. 2014. *Adv. Mater.* 26(34):5936–41
6. Chen P, Güven S, Usta OB, Yarmush ML, Demirci U. 2015. *Adv. Healthcare Mater.* 4(13):1937–43
7. Guven S, Chen P, Inci F, Tasoglu S, Erkmén B, Demirci U. 2015. *Trends Biotechnol.* 33(5):269–79
8. Tsai C, Mao R, Lin S, Zhu Y, Tsai S. 2014. *Technology* 2(1):75–81
9. Marthelot J, Strong E, Reis PM, Brun PT. 2018. *Nat. Commun.* 9(1):4477
10. Brun PT. 2022. *JACS Au* 2(11):2417–25
11. Truby RL, Lewis JA. 2016. *Nature* 540(7633):371–78
12. Bico J, Reyssat É, Roman B. 2018. *Annu. Rev. Fluid Mech.* 50:629–59
13. Andreotti B, Snoeijer JH. 2020. *Annu. Rev. Fluid Mech.* 52:285–308
14. Shuttleworth R. 1950. *Proc. Phys. Soc. Lond. Sec. A* 63(5):444–57
15. Style RW, Jagota A, Hui CY, Dufresne ER. 2017. *Annu. Rev. Condens. Matter Phys.* 8:99–118
16. Müller P, Saül A. 2004. *Surf. Sci. Rep.* 54(5–8):157–258
17. Xu Q, Jensen KE, Boltysanskiy R, Sarfati R, Style RW, Dufresne ER. 2017. *Nat. Commun.* 8(1):555
18. Xu Q, Style RW, Dufresne ER. 2018. *Soft Matter* 14(6):916–20
19. Schulman RD, Trejo M, Salez T, Raphaël E, Dalnoki-Veress K. 2018. *Nat. Commun.* 9(1):982
20. Ogden R. 1997. *Nonlinear Elastic Deformations*. Chichester, Engl.: Dover Publ.
21. Mora S, Pomeau Y. 2017. In *Soft Interfaces: Lecture Notes Les Houches Summer School: Volume 98, July 2012*, ed. L Bocquet, D Quéré, TA Witten, LF Cugliandolo, pp. 189–220. Oxford, UK: Oxford Acad.
22. Gurtin ME, Murdoch AI. 1978. *Int. J. Solids Struct.* 14(6):431–40
23. Chen T, Chiu MS, Weng CN. 2006. *J. Appl. Phys.* 100(7):074308
24. Landau LD, Lifshitz EM. 2013. *Fluid Mechanics*, Vol. 6, *Course of Theoretical Physics*. Oxford, UK: Pergamon
25. Ó-Bryan CS, Brady-Miné A, Tessmann CJ, Spatz AM, Angelini TE. 2021. *Soft Matter* 17(14):3886–94
26. Plateau JAF. 1873. *Experimental and Theoretical Statics of Liquids Subject to Molecular Forces Only*, Vol. 2. Paris: Gauthier-Villars
27. Rayleigh L. 1878. *Proc. Lond. Math. Soc.* 1(1):4–13
28. Rayleigh L. 1879. *Proc. R. Soc. Lond.* 29(196–199):71–97
29. Mora S, Phou T, Fromental JM, Pismen LM, Pomeau Y. 2010. *Phys. Rev. Lett.* 105(21):214301
30. Mora S, Andò E, Fromental JM, Phou T, Pomeau Y. 2019. *Soft Matter* 15(27):5464–73
31. Mora S, Abkarian M, Tabuteau H, Pomeau Y. 2011. *Soft Matter* 7(22):10612–19
32. van Limbeek MA, Essink MH, Pandey A, Snoeijer JH, Karpitschka S. 2021. *Phys. Rev. Lett.* 127(2):028001
33. Taffetani M, Ciarletta P. 2015. *J. Mech. Phys. Solids* 81:91–120
34. Taffetani M, Ciarletta P. 2015. *Phys. Rev. E* 91(3):032413
35. Xuan C, Biggins J. 2016. *Phys. Rev. E* 94(2):023107
36. Xuan C, Biggins J. 2017. *Phys. Rev. E* 95(5):053106
37. Lestringant C, Audoly B. 2020. *Proc. R. Soc. A* 476(2240):20200337
38. Fu Y, Jin L, Goriely A. 2021. *J. Mech. Phys. Solids* 147:104250
39. Wang Q, Liu M, Wang Z, Chen C, Wu J. 2021. *J. Appl. Mech.* 88(4):041010
40. Dortdivanlioglu B, Javili A. 2022. *Extreme Mech. Lett.* 55:101797
41. Biot MA. 1963. *Appl. Sci. Res.* 12(2):168–82
42. Cai S, Chen D, Suo Z, Hayward RC. 2012. *Soft Matter* 8(5):1301–4
43. Tällinen T, Chung JY, Biggins JS, Mahadevan L. 2014. *PNAS* 111(35):12667–72
44. Jin L, Cai S, Suo Z. 2011. *EPL* 95(6):64002
45. Dervaux J, Amar MB. 2012. *Annu. Rev. Condens. Matter Phys.* 3(1):311–32
46. Liu Q, Ouchi T, Jin L, Hayward R, Suo Z. 2019. *Phys. Rev. Lett.* 122(9):098003
47. Essink MH, van Limbeek MA, Pandey A, Karpitschka S, Snoeijer JH. 2023. *Soft Matter* 19(27):5160–68
48. Paretkar D, Xu X, Hui CY, Jagota A. 2014. *Soft Matter* 10(23):4084–90
49. Mora S, Pomeau Y. 2015. *J. Phys. Condens. Matter* 27(19):194112
50. Mora S, Maurini C, Phou T, Fromental JM, Audoly B, Pomeau Y. 2013. *Phys. Rev. Lett.* 111(11):114301
51. Molefe L, Kolinski JM. 2023. *Phys. Rev. E* 108(4):L043001
52. Hui CY, Liu Z, Bain N, Jagota A, Dufresne ER, et al. 2020. *Proc. R. Soc. A* 476(2243):20200477
53. Berman JD, Randeria M, Style RW, Xu Q, Nichols JR, et al. 2019. *Soft Matter* 15(6):1327–34

54. Barnes HA. 2000. *A Handbook of Elementary Rheology*. Aberystwyth, UK: Univ. Wales Inst. Non-Newtonian Fluid Mech.
55. McKinley GH. 2005. *Dimensionless groups for understanding free surface flows of complex fluids*. HML Rep. No. 05-P-05, Hatsopoulos Microfluidics Lab., Dep. Mech. Eng., MIT, Cambridge, MA. <http://web.mit.edu/nmf/publications/GHM78.pdf>
56. Wang J, Joseph DD, Funada T. 2005. *J. Non-Newtonian Fluid Mech.* 129(2):106–16
57. Ji S, Guvendiren M. 2017. *Front. Bioeng. Biotechnol.* 5:23
58. Suntornnond R, An J, Chua CK. 2017. *Macromol. Mater. Eng.* 302(1):1600266
59. Rayleigh L. 1885. *Proc. Lond. Math. Soc.* 1(1):4–11
60. Lamb H. 1932. *Hydrodynamics*. Cambridge, UK: Cambridge Univ. Press
61. Harden J, Pleiner H, Pincus P. 1991. *J. Chem. Phys.* 94(7):5208–21
62. Onodera Y, Choi PK. 1998. *J. Acoust. Soc. Am.* 104(6):3358–63
63. Monroy F, Langevin D. 1998. *Phys. Rev. Lett.* 81(15):3167–70
64. Shao X, Saylor JR, Bostwick JB. 2018. *Soft Matter* 14(36):7347–53
65. Zheng Y, Lai Y, Hu Y, Cai S. 2019. *J. Mech. Phys. Solids* 131:221–29
66. Slutzky M, Hwang J, Stone HA, Nunes JK. 2023. *Langmuir* 40(2):1567–75
67. Shao X, Bevilacqua G, Ciarletta P, Saylor JR, Bostwick JB. 2020. *Phys. Rev. E* 102(6):060602
68. Monroy F. 2017. *Adv. Colloid Interface Sci.* 247:4–22
69. Chantelot P, Domino L, Eddi A. 2020. *Phys. Rev. E* 101(3):032609
70. Shao X, Wilson P, Saylor JR, Bostwick JB. 2021. *J. Fluid Mech.* 915:A19
71. Shao X, Wilson P, Bostwick JB, Saylor JR. 2021. *J. Fluid Mech.* 919:A18
72. Wilson P, Shao X, Saylor JR, Bostwick JB. 2022. *Phys. Rev. Fluids* 7(1):014803
73. Rayleigh L. 1882. *Proc. Lond. Math. Soc.* s1-14(1):170–77
74. Taylor GI. 1950. *Proc. R. Soc. Lond. Ser. A* 201(1065):192–96
75. Sharp DH. 1984. *Phys. D Nonlinear Phenom.* 12(1–3):3–18
76. Mora S, Phou T, Fromental JM, Pomeau Y. 2014. *Phys. Rev. Lett.* 113(17):178301
77. Tamim SI, Bostwick JB. 2020. *Extreme Mech. Lett.* 40:100940
78. Tahir NA, Hoffmann DHH, Kozyreva A, Tauschwitz A, Shutov A, et al. 2000. *Phys. Rev. E* 63(1):016402
79. Terrones G. 2005. *Phys. Rev. E* 71(3):036306
80. Piriz A, Cela JL, Cortazar O, Tahir N, Hoffmann D. 2005. *Phys. Rev. E* 72(5):056313
81. Piriz AR, López Cela JJ, Tahir NA. 2009. *J. Appl. Phys.* 105(11):116101
82. Gou J, Zeng R, Wang C, Sun Y. 2022. *AIP Adv.* 12(7):075217
83. Li K, Zhuo G, Zhang Y, Liu C, Chen W, Lü C. 2022. *Extreme Mech. Lett.* 55:101809
84. Tamim SI, Bostwick JB. 2021. *Soft Matter* 17(15):4170–79
85. Pandey A, Kansal M, Herrada MA, Eggers J, Snoeijer JH. 2021. *Soft Matter* 17(20):5148–61
86. Faraday M. 1831. *Philos. Trans. R. Soc. Lond. Ser. A* 121:299–340
87. Matthiessen L. 1868. *Ann. Phys.* 210(5):107–17
88. Rayleigh L. 1883. *Philos. Mag.* 16:50–58
89. Benjamin TB, Ursell FJ. 1954. *Proc. R. Soc. Lond. Ser. A* 225:505–15
90. Wright P, Saylor J. 2003. *Rev. Sci. Instrum.* 74(9):4063–70
91. Strickland SL, Shearer M, Daniels KE. 2015. *J. Fluid Mech.* 777:523–43
92. Melo F, Umbanhowar P, Swinney HL. 1994. *Phys. Rev. Lett.* 72(1):172–75
93. Briard A, Gostiaux L, Gréa B-J. 2020. *J. Fluid Mech.* 883:A57
94. Miles J, Henderson D. 1990. *Annu. Rev. Fluid Mech.* 22:143–65
95. Kumar K, Tuckerman LS. 1994. *J. Fluid Mech.* 279:49–68
96. Kumar K. 1996. *Proc. R. Soc. Lond. Ser. A* 452(1948):1113–26
97. Raynal F, Kumar S, Fauve S. 1999. *Eur. Phys. J. B* 9:175–78
98. Wagner C, Müller H, Knorr K. 1999. *Phys. Rev. Lett.* 83(2):308–11
99. Müller H, Zimmermann W. 1999. *EPL* 45(2):169–74
100. Kumar S. 1999. *Phys. Fluids* 11(8):1970–81
101. Bevilacqua G, Shao X, Saylor JR, Bostwick JB, Ciarletta P. 2020. *Proc. R. Soc. A* 476(2241):20200129
102. Miller C, Scriven L. 1968. *J. Fluid Mech.* 32:417–35

103. Prosperetti A. 1980. *J. Mec.* 19:149–82
104. Tsamopoulos J, Brown R. 1983. *J. Fluid Mech.* 127:519–37
105. Trinh E, Wang T. 1982. *J. Fluid Mech.* 122:315–38
106. Wang T, Anilkumar A, Lee C. 1996. *J. Fluid Mech.* 308:1–14
107. Lamb H. 1881. *Proc. Lond. Math. Soc.* s1-13(1):189–212
108. Chree C. 1889. *Trans. Camb. Philos. Soc.* 14:250–69
109. Sato Y. 1962. *Geophys. Mag.* 31:15–24
110. Eringen AC, Suhubi ES, Chao CC. 1975. *Elastodynamics*, Vol. 2, *Linear Theory*. New York: Academic
111. Shao X, Fredericks SA, Saylor JR, Bostwick JB. 2019. *Phys. Rev. Lett.* 123(18):188002
112. Bastrukov SI. 1994. *Phys. Rev. E* 49(4):3166–70
113. Steen PH, Chang CT, Bostwick JB. 2019. *PNAS* 116(11):4849–54
114. Chakrabarti A, Chaudhury MK. 2014. *Extreme Mech. Lett.* 1:47–53
115. Trinh E, Marston P, Robey J. 1988. *J. Colloid Interface Sci.* 124(1):95–103
116. Tian Y, Holt RG, Apfel RE. 1995. *Phys. Fluids* 7(12):2938–49
117. Tian Y, Holt RG, Apfel RE. 1997. *J. Colloid Interface Sci.* 187(1):1–10
118. Kremer J, Kilzer A, Petermann M. 2018. *Rev. Sci. Instrum.* 89(1):015109
119. Hosseinzadeh VA, Brugnara C, Holt RG. 2018. *Sci. Rep.* 8(1):16794
120. Shao X, Fredericks SA, Saylor JR, Bostwick JB. 2020. *J. Acoust. Soc. Am.* 147(4):2488–98
121. Hosseinzadeh VA, Holt RG. 2017. *J. Appl. Phys.* 121:174502
122. Marston PL. 1980. *J. Acoust. Soc. Am.* 67:15–26
123. Tamim SI, Bostwick JB. 2019. *Soft Matter* 15(45):9244–52
124. Tamim SI, Bostwick JB. 2021. *NPJ Microgravity* 7(1):42
125. Pandey A, Andreotti B, Karpitschka S, van Zwieten G, van Brummelen EH, Snoeijer JH. 2020. *Phys. Rev. X* 10(3):031067
126. Masurel R, Roché M, Limat L, Ionescu I, Dervaux J. 2019. *Phys. Rev. Lett.* 122(24):248004
127. Bain N, Jagota A, Smith-Mannschott K, Heyden S, Style RW, Dufresne ER. 2021. *Phys. Rev. Lett.* 127(20):208001
128. Carbonaro A, Chagua-Encarnacion KN, Charles CA, Phou T, Ligoure C, et al. 2020. *Soft Matter* 16(36):8412–21
129. Zafar MR, Basu S. 2021. *Phys. Rev. E* 103(6):063003
130. Heyden S, Vlahovska PM, Dufresne ER. 2022. *J. Mech. Phys. Solids* 161:104786
131. Jaspers M, Dennison M, Mabesoone MF, MacKintosh FC, Rowan AE, Kouwer PH. 2014. *Nat. Commun.* 5(1):5808
132. Luo J, Li S, Xu J, Chai M, Gao L, et al. 2021. *Adv. Funct. Mater.* 31(43):2104139
133. Pajic-Lijakovic I, Eftimie R, Milivojevic M, Bordas SPA. 2023. *Adv. Colloid Interface Sci.* 315:102902
134. Hobson EC, Li W, Juliar BA, Putnam AJ, Stegemann JP, Deng CX. 2021. *Biomaterials* 269:120676
135. Snoeijer J, Pandey A, Herrada M, Eggers J. 2020. *Proc. R. Soc. A* 476(2243):20200419
136. Charru F. 2011. *Hydrodynamic Instabilities*, Vol. 37. Cambridge, UK: Cambridge Univ. Press
137. Scriven L, Sternling C. 1960. *Nature* 187(4733):186–88
138. Vuilleumier R, Ego V, Neltner L, Cazabat A. 1995. *Langmuir* 11(10):4117–21
139. Yadav V, Yousafzai MS, Amiri S, Style RW, Dufresne ER, Murrell M. 2022. *Phys. Rev. Fluids* 7(3):L031101
140. Pajic-Lijakovic I, Milivojevic M. 2022. *Eur. Biophys. J.* 51(6):419–29
141. Riccobelli D. 2021. *Phys. Rev. E* 104(2):024417
142. Louf JF, Kratz F, Datta SS. 2020. *Phys. Rev. Res.* 2(4):043382
143. Salbreux G, Jülicher F. 2017. *Phys. Rev. E* 96(3):032404
144. Binysh J, Wilks TR, Souslov A. 2022. *Sci. Adv.* 8(10):eabk3079
145. França HL, Jalaal M, Oishi CM. 2024. *Phys. Rev. Res.* 6(1):013226
146. Ha J, Kim HY. 2020. *Annu. Rev. Fluid Mech.* 52:263–84